

# A universal moiré effect and application in X-ray phase-contrast imaging

Houxun Miao<sup>1\*</sup>, Alireza Panna<sup>1</sup>, Andrew A. Gomella<sup>2</sup>, Eric E. Bennett<sup>1</sup>, Sami Znati<sup>1</sup>, Lei Chen<sup>3</sup> and Han Wen<sup>1\*</sup>

**A moiré pattern results from superimposing two black-and-white or greyscale patterns of regular geometry, such as two sets of evenly spaced lines. Here, we report the observation of an analogous effect with two transparent phase masks put in a light beam. The phase moiré effect and the classic moiré effect are shown to be the two ends of a continuous spectrum. The former allows the detection of sub-resolution intensity or phase patterns with a transparent screen. When applied to X-ray imaging, it enables the realization of a polychromatic far-field interferometer (PFI) without the need for absorption gratings. X-ray interferometry can non-invasively detect refractive index variations inside an object<sup>1–10</sup>. Current bench-top interferometers operate in the near field with limitations in sensitivity and X-ray dose efficiency<sup>2,5,7–10</sup>. The universal moiré effect helps overcome these limitations and obviates the need for using hard X-ray absorption gratings with sub-micrometre periods.**

The classic moiré effect is the product of two intensity patterns of slightly different sizes or orientations. It can be found in a variety of forms in diverse applications, including metrology, precision measurements, alignment and imaging<sup>11–13</sup>. Transparent phase masks, or phase gratings, imprint a periodic phase pattern on a wavefront. When two such gratings are overlaid in a light beam, there is no moiré effect immediately behind the gratings in the near field; we did, however, observe an achromatic intensity pattern in the far field. Its spatial frequency equals the difference between the projected frequencies of the two gratings. The two gratings can either be in contact or have a finite spacing. We show that this phase moiré effect and the classic effect are the extremes of a general effect for masks that mix phase and amplitude modulations to various degrees.

In the experiment illustrated in Fig. 1a, two identical visible-light phase gratings of the same 14.3  $\mu\text{m}$  period ( $G_1$  and  $G_2$ ) were overlaid in parallel planes. They were illuminated by a white-light cone beam from a source of 0.44 mm size and projected onto a frosted-glass image screen (see Supplementary Fig. 1 for a photo of the set-up, the light spectrum and the phase-shift profile of the gratings). The geometric distances were  $L_1 = 18.0$  cm from the source to the first grating,  $L_2$  varying between 5 mm and 20.5 cm from the second grating to the image screen, and the inter-grating spacing  $D$  fixed at 0.41 mm. Broad intensity fringes emerged as the image screen moved away from the gratings (Fig. 1b). Supplementary Movie 1 shows the full images when scanning the position of the image screen.

An intuitive explanation of the phase moiré effect is illustrated in Fig. 1c. The cone beam projects the self-images of  $G_1$  onto the plane of  $G_2$  with a slightly magnified period  $P_1$  (ref. 14),

resulting approximately in a combined phase oscillation of the form  $\phi[\cos(2\pi x/P_1) + \cos(2\pi x/P_2)]$ , where  $P_2$  is the period of  $G_2$ . It can be written as  $2\phi \cos[\pi x(1/P_1 - 1/P_2)] \cos[\pi x(1/P_1 + 1/P_2)]$ , which is equivalent to a single phase grating whose phase shift is modulated by a beat pattern. The beat pattern represents alternating strongly and weakly diffracting areas. Light that is transmitted through the strongly diffracting areas is diverted into side diffraction orders and away from the direction of straight radial projection. After a sufficient distance, the redirection of the flux gives rise to periodic intensity fringes, as shown in Fig. 1c. The measured and theoretical dependence of the fringe visibility on the position of the image screen are summarized in Fig. 1d. Fringe visibility is fringe amplitude/mean intensity, or  $(I_{\max} - I_{\min})/(I_{\max} + I_{\min})$ .

The moiré carpet in Fig. 2a shows experimentally the progression of the moiré fringes with the inter-grating spacing  $D$  in the range from 0.05 mm and 5 mm. The image screen was fixed at 20 cm from the source. The gratings were placed midway between them. As  $D$  increases, the difference in the projected frequencies of the gratings also increases, leading to denser fringes. Coherent interference between different diffraction orders occurs in the space between the gratings, producing the appropriate self-images of  $G_1$  at the  $G_2$  plane at regular intervals<sup>14</sup> of  $D$ . Therefore, the fringe contrast underwent a periodic oscillation and gradually diminished with increasing  $D$  owing to the broad spectrum of the light. The interval of oscillation is theoretically<sup>14</sup>  $2P^2/\lambda$ . The measured value of  $0.74 \pm 0.09$  mm matches the 550 nm average wavelength of the white-light spectrum (Supplementary Fig. 1). The measured and theoretically calculated fringe visibilities as a function of the spacing  $D$  are shown in Fig. 2b. The measured fringe spatial frequency as a function of  $D$  is also predictable by theory (Fig. 2b). Supplementary Movie 2 shows the full images when scanning  $D$ .

The theoretical derivation of the general situation of a polychromatic cone beam illuminating a pair of gratings of different periods is provided in Methods. The phase moiré effect and the classic moiré effect are at the two extremes. With pure amplitude gratings the classic moiré effect appears immediately behind the gratings. There is no requirement on the lateral coherence of the light source. With pure phase gratings the phase moiré effect appears at a distance from the gratings; the lateral coherence of the light at the first grating should be approximately the period of the grating. A continuous transition exists between the two extremes for any combination of intensity and phase modulations.

For phase-contrast imaging applications that require high sensitivity, the space between the gratings can be the preferred location to place the objects, because coherent wave interference

<sup>1</sup>Biophysics and Biochemistry Center, National Heart, Lung and Blood Institute, National Institutes of Health, Bethesda, Maryland 20892, USA.

<sup>2</sup>Sidney Kimmel Medical College, Thomas Jefferson University, Philadelphia, Pennsylvania 19107, USA. <sup>3</sup>Center for Nanoscale Science and Technology, National Institute of Standards and Technology, Gaithersburg, Maryland 20899, USA. \*e-mail: [miaoh@mail.nih.gov](mailto:miaoh@mail.nih.gov); [wenh@nhlbi.nih.gov](mailto:wenh@nhlbi.nih.gov)

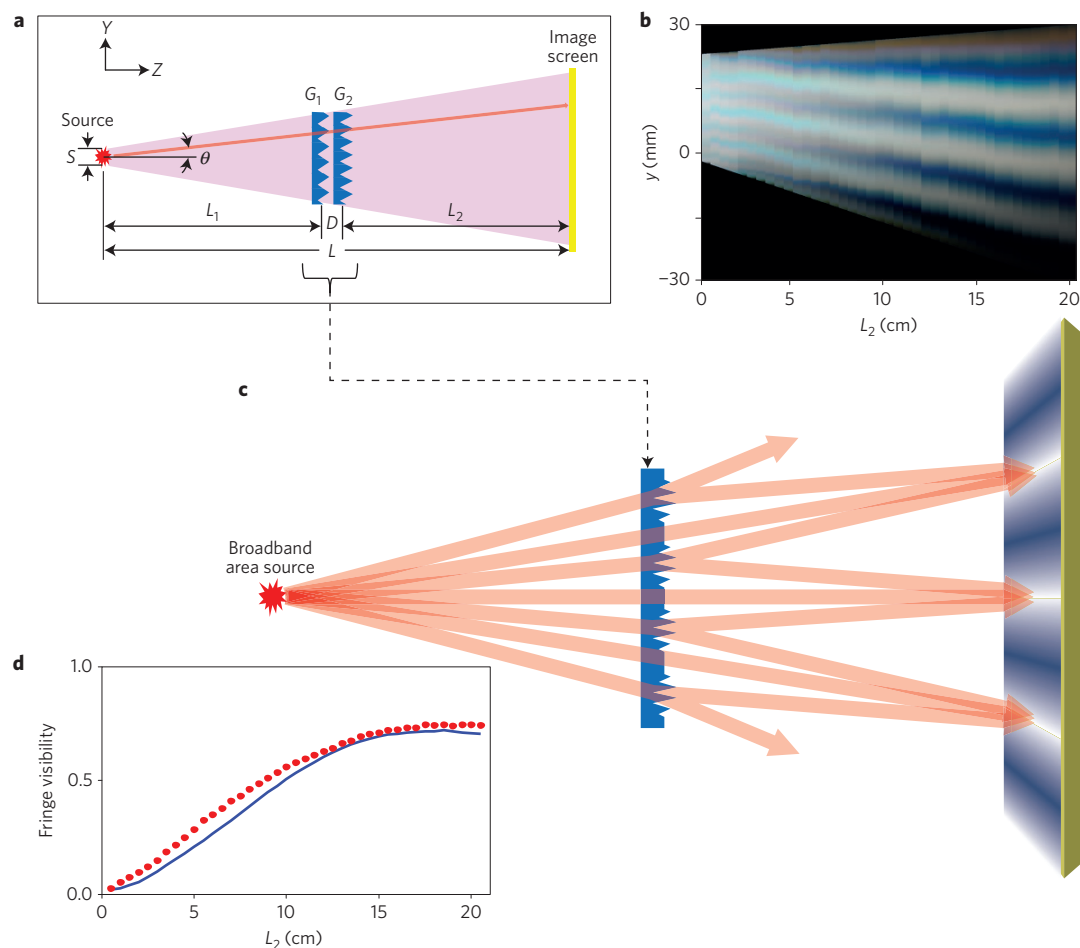


**Figure 1 | An example of the phase moiré effect between two transparent phase gratings.** **a**, A white-light source of a finite size illuminates the gratings. A frosted-glass screen captures the projected colour image. **b**, The vertical cross-section of the image as a function of the grating-to-screen distance  $L_2$  shows a moiré pattern arising at a distance. Supplementary Fig. 1 includes a photo of the experimental set-up and Supplementary Movie 1 shows the full images. **c**, The explanation is that the two gratings act as a single phase grating whose phase oscillation is modulated by a beat pattern, representing interleaved strongly and weakly diffracting areas. Photons transmitted through the strongly diffracting areas are diffracted away from the direction of straight radial projection, giving rise to intensity bands at a distant plane. **d**, Dependence of measured (red dots) and theoretically calculated (blue line) fringe visibility on the distance  $L_2$ . Measurement uncertainty was 0.003.

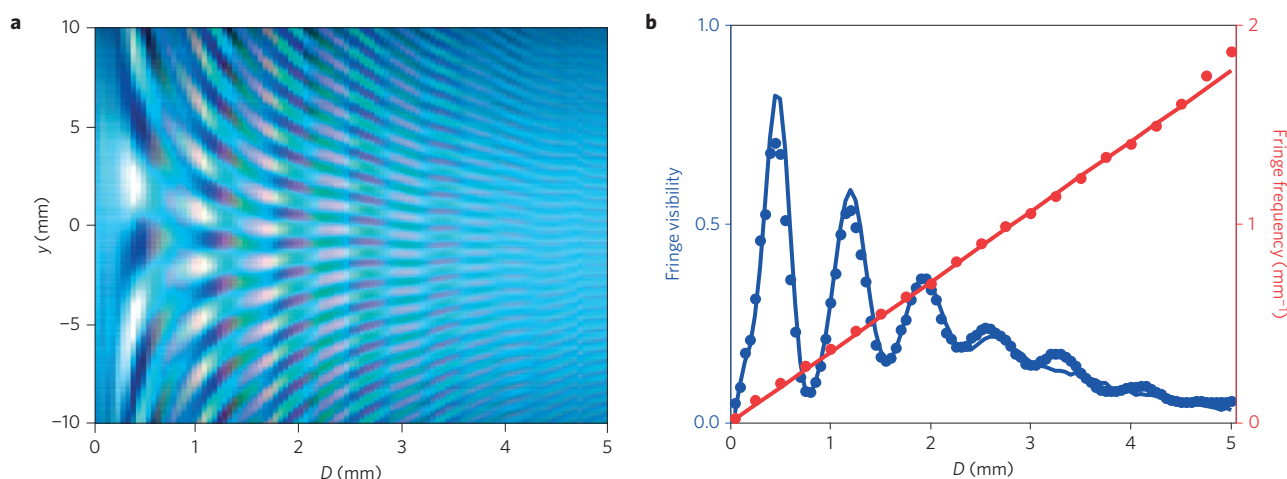


**Figure 2 | Dependence of the moiré pattern on the inter-grating spacing in the set-up shown in Fig. 1.** **a**, In the moiré carpet, the fringe pattern at a given inter-grating spacing  $D$  is shown as a vertical strip. The strips for the range of  $D$  values are stitched into the carpet. **b**, Quantitative comparison of the moiré fringe visibility (blue) and spatial frequency (red) between theoretical calculations (solid lines) and experimental results (dots), as functions of the spacing  $D$ . The measurement uncertainty of fringe visibility was 0.003 and the measurement uncertainty of fringe frequency was  $0.05 \text{ mm}^{-1}$ .

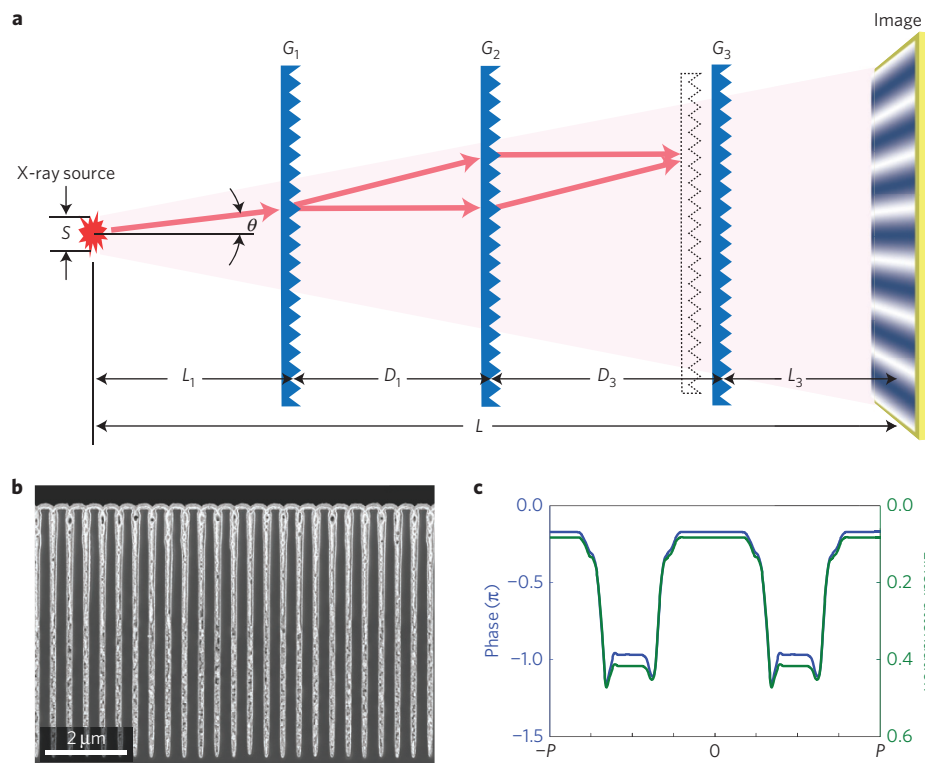


**Figure 3 | The moiré effect among three phase gratings underlies a polychromatic far-field interferometer in this X-ray example. a**, Under a cone beam the first two gratings form a series of achromatic interference patterns at a plane downstream. The third grating is positioned on or near the plane to form moiré fringes at a distance. **b**, SEM image of a cross-section of the phase grating  $G_1$ . Trenches in silicon are filled with gold to create a periodic profile of phase shift. **c**, The grating SEM cross-sections were used to calculate their phase-shift and linear attenuation profiles. Data of the  $G_1$  grating at 27.5 keV are shown. The sharp dips are produced by a thin layer of Pt.

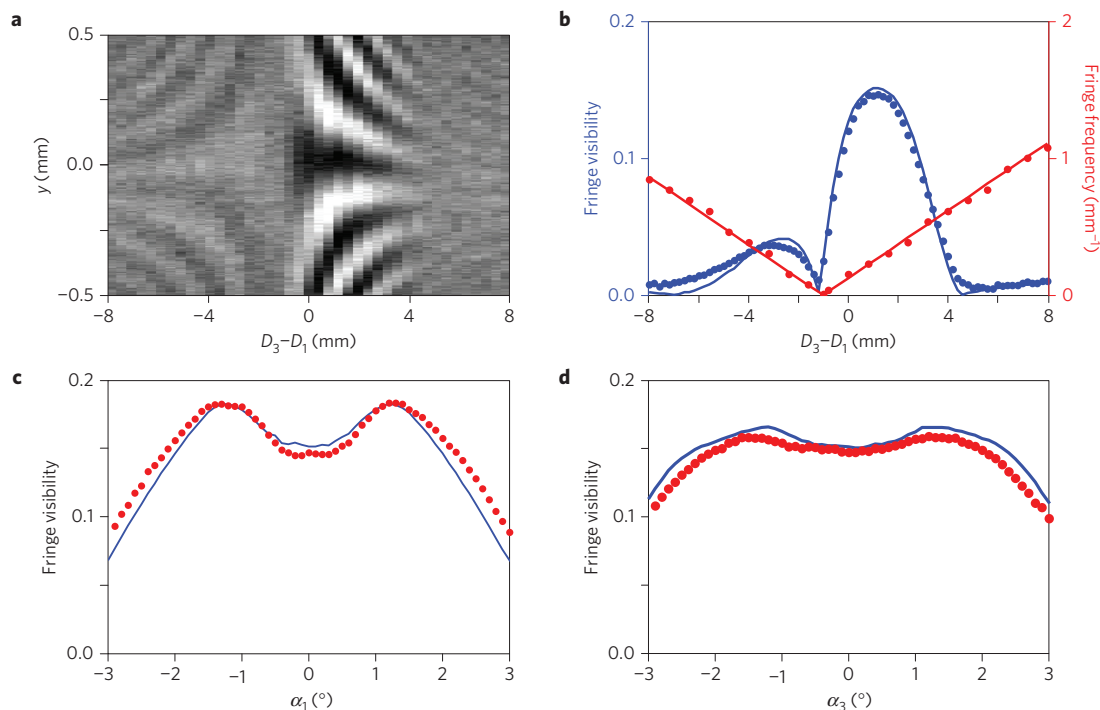


**Figure 4 | Experimental data from the X-ray polychromatic far-field interferometer with mismatched grating periods. a**, The moiré carpet shows the evolution of the fringe pattern as the longitudinal position of the third grating is scanned. **b**, Quantitative comparison of the fringe visibility (blue) and spatial frequency (red) between theoretical calculations (solid lines) and measurements (dots), as functions of the position of the  $G_3$  grating. The measurement uncertainty of fringe visibility was 0.005 and the measurement uncertainty of fringe frequency was  $0.05\ \text{mm}^{-1}$ . **c**, Theoretical (solid blue line) and measured (red dots) fringe visibilities as a function of the out-of-plane tilt of the grating  $G_1$ . **d**, The same comparison for the  $G_3$  grating. The peak fringe visibility of 19.4% was reached by optimizing both grating position and tilts.

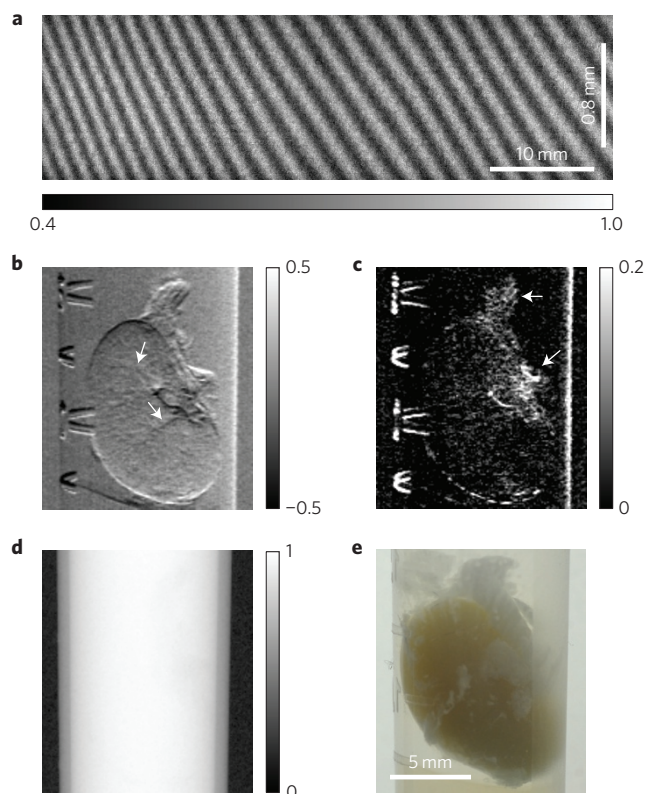


**Figure 5 | Multimodal X-ray projection images of a mouse kidney specimen immersed in water.** **a**, A single shot image of the grating area without the specimen shows the moiré fringes. Grey scale is the normalized image intensity. **b**, The differential phase image reveals the outline and internal blood vessels (white arrows) of the kidney, together with the graduation marks on the centrifuge tube. Grey scale is in radians. **c**, The decoherence image shows reduced moiré fringe amplitude in fatty tissue (white arrows) and at the edges of the graduation marks. Grey scale is the linear attenuation coefficient. **d**, Conventional attenuation-contrast radiography shows the fatty tissue as darker areas indicating lower density. Grey scale is the linear attenuation coefficient. **e**, A photograph of the kidney specimen suspended in water in the centrifuge tube.

occurs here. With this in mind, a three-grating set-up (Fig. 3a) has the advantage that it allows the gratings to be widely separated. Here, the  $G_2$  grating refocuses the diffracted waves from  $G_1$  into a series of achromatic Fourier images at a specific plane downstream<sup>14</sup>. The  $G_3$  grating is placed on or near this plane to produce moiré effects between itself and the Fourier images. See Methods for the theoretical formulae of the three-grating set-up. Similar to the two-grating system, the  $G_1$  grating can be a pure intensity or a pure phase grating as the two extreme cases. The former allows an extended light source with minimal lateral coherence, but at the cost of light reduction by  $G_1$ ; the latter requires the lateral coherence of the source at  $G_1$  to be approximately the grating period.

The phase moiré effect is now recognized as the underlying mechanism of a type of X-ray interferometer that uses only phase gratings, which has previously demonstrated an order of magnitude increase in sensitivity and reduction in radiation dose when compared with the current Talbot–Lau interferometer<sup>15</sup>. This understanding leads to the use of purposely mismatched grating periods to substantially improve the efficiency of the X-ray polychromatic far-field interferometer. The improved design has three phase gratings of 1 mm by 7 cm area and periods of 399 nm, 400 nm and 400 nm, respectively. Grating fabrication is described in ref. 16. The X-ray tube had a rhenium–tungsten anode

and operated at 40 kVp/40 mA. A 70- $\mu$ m-wide slit was placed on the X-ray tube window to limit the vertical size of the source while keeping sufficient angular spread of the beam to cover the grating area. See Supplementary Fig. 2 for a photo of the system. The geometric distances illustrated in Fig. 3a were  $L_1 = 0.391$  m,  $D_1 = 0.463$  m,  $L_3 = 0.710$  m. The distance  $D_3$  was scanned over the range  $D_1 \pm 8$  mm. The cross-section profiles of the gratings (Fig. 3b) were obtained with scanning electron microscopy (SEM). The gratings are designed for phase shifting but also contain material absorption. From these profiles both the phase-shift and linear attenuation profiles were extracted for photon energies of 20–40 keV (data at 27.5 keV are plotted in Fig. 3c). The  $G_2$  profile was designed to maximize light diffraction into the  $\pm 1$  orders.

The moiré carpet in Fig. 4a shows the evolution of the moiré fringes with changing  $G_3$  position. Full-field images are provided in Supplementary Movie 3. The measured and theoretically calculated fringe visibility and frequency curves are shown in Fig. 4b for the case of parallel grating planes. The fringe visibility increased with out-of-plane tilting of the gratings. With  $G_3$  positioned at  $D_3 - D_1 = 1.2$  mm, the measured and theoretically calculated fringe visibility curves as functions of the tilt angles of  $G_1$  and  $G_3$  are shown in Fig. 4c,d, respectively. The out-of-plane tilt mainly altered the transmission profiles of the gratings. Their influence on the fringe contrast is discussed in Methods. The peak fringe visibility of 19.4% was attained when both  $G_1$  and  $G_3$  were tilted at  $1.2^\circ$ . This is a 43% increase in fringe visibility over the previous 13.5% value<sup>15</sup> owing to the use of mismatched grating periods.

In imaging experiments the samples are positioned behind grating  $G_2$  (Fig. 3a), where vertically separated light paths coherently interfere. A local gradient of the refractive index creates a phase shift of the moiré fringes. An image of the phase shift is a differential phase image. A second measurement is the attenuation of the fringe amplitude due to perturbations by the object that reduce the mutual coherence of the light paths. This provides a decoherence image. The raw projection images were taken in a phase-stepping procedure<sup>7,8,17</sup> and processed with an adaptive algorithm to deal with mechanical fluctuations. A complete data set included ten images of 1 s exposure each, at a total entrance surface radiation dose (ESD) of 0.71 mGy. The grating area determined a 0.7 mm by 5 cm field of view at the sample. Samples were scanned in steps of 0.7 mm, and multiple fields of view were tiled to cover the desired height.

Figure 5a shows a reference image without any sample. It is stretched in the vertical direction owing to an oblique incident angle of  $4.5^\circ$  of the beam on the detector screen for improved efficiency and vertical resolution<sup>18</sup>. The grating  $G_3$  was slightly rotated around the beam axis to produce an inclination of the fringes from the horizontal direction. Figure 5b–d are multimodal projection images of a formalin-fixed, unstained mouse kidney specimen immersed in water, including the differential phase, decoherence and conventional attenuation-contrast radiography. Although a single projection, the outline and internal blood vessels of the kidney become visible in the differential phase image (Fig. 5b). The accompanying decoherence image (Fig. 5c) shows reduced coherence in the peripheral fat tissue (white arrows) and also in areas containing steep gradients of the differential phase, such as the bright edges of the graduation marks on the centrifuge tube. This is caused by a large dispersion of the fringe phase within a pixel<sup>19</sup>. The conventional radiography (Fig. 5d) was taken with a flat-panel X-ray detector at a dose of 4.47 mGy ESD. A photograph of the specimen is shown in Fig. 5e.

Generally when creating a distant moiré pattern with a phase grating, the fringe period scales inversely with the grating period (see equation (17) in Methods). Therefore, smaller grating periods allow shorter observation distances. In ideal situations, the moiré fringe visibility between two phase gratings and among three phase gratings are estimated at 81% and 33%, respectively. Practically the



visibility is reduced by less than ideal grating profiles, scattering in the grating material, spectral dispersion of the grating phase shift with a broadband source and the detector resolution.

Although the self-imaging of gratings is a coherent interference effect<sup>20</sup>, the universal moiré effect is at its core an incoherent intensity effect. With highly coherent sources such as a point monochromatic source, the self or Fourier images of gratings may coexist with the moiré effect in the form of fine fringes superimposed on broad moiré patterns. The moiré effect between phase masks still requires a certain level of lateral coherence of the illumination, because the effect appears at a standoff distance from the masks. It is shown in Methods that the lateral coherence length of the illumination at the first phase grating should be comparable to the grating period. On the other hand, a first amplitude grating segments the incident beam and removes the coherence requirement on the illumination similar to the Lau effect, which is detailed in Methods.

Owing to its simplicity and robustness towards environmental factors, the phase moiré effect was recently implemented for polychromatic and monochromatic cold neutron sources in quantum information and imaging research using pure silicon gratings as phase masks (D. S. Hussey, D. A. Pushin, M. G. Huber and D. L. Jacobson, manuscript in preparation). In a broad sense the universal moiré effect occurs when a periodic screen is placed on a periodically modulated wavefront. The periodic wavefront can be the Fourier image of other grating(s) upstream. The classic moiré effect is a special case where the screen is an intensity mask. Our finding shows that one can use a phase mask as the screen. The effect also occurs for pure phase modulations which are not visible by direct observation of the intensity distribution.

## Methods

Methods and any associated references are available in the [online version of the paper](#).

Received 20 October 2015; accepted 15 March 2016;  
published online 25 April 2016

## References

1. Bonse, U. & Hart, M. An X-ray interferometer. *Appl. Phys. Lett.* **6**, 155–156 (1965).
2. Clauser, J. F. & Li, S. F. Talbot–Von Lau atom interferometry with cold slow potassium. *Phys. Rev. A* **49**, R2213–R2216 (1994).
3. Momose, A., Takeda, T., Itai, Y. & Hirano, K. Phase-contrast X-ray computed tomography for observing biological soft tissues. *Nature Med.* **2**, 473–475 (1996).
4. Cloetens, P., Guigay, J. P., DeMartino, C., Baruchel, J. & Schlenker, M. Fractional Talbot imaging of phase gratings with hard X-rays. *Opt. Lett.* **22**, 1059–1061 (1997).
5. Clauser, J. F. Ultrahigh resolution interferometric X-ray imaging. US patent 5,812,629 (1998).
6. David, C., Nohammer, B., Solak, H. H. & Ziegler, E. Differential X-ray phase contrast imaging using a shearing interferometer. *Appl. Phys. Lett.* **81**, 3287–3289 (2002).
7. Momose, A. *et al.* Demonstration of X-ray Talbot interferometry. *Jpn. J. Appl. Phys.* **42**, L866–L868 (2003).
8. Weitkamp, T. *et al.* X-ray phase imaging with a grating interferometer. *Opt. Express* **13**, 6296–6304 (2005).
9. Pfeiffer, F., Weitkamp, T., Bunk, O. & David, C. Phase retrieval and differential phase-contrast imaging with low-brilliance X-ray sources. *Nature Phys.* **2**, 258–261 (2006).
10. Pfeiffer, F. *et al.* Hard-X-ray dark-field imaging using a grating interferometer. *Nature Mater.* **7**, 134–137 (2008).
11. Reid, G. T. Moiré fringes in metrology. *Opt. Lasers Eng.* **5**, 63–93 (1984).
12. Gustafsson, M. G. L. Surpassing the lateral resolution limit by a factor of two using structured illumination microscopy. *J. Microsc.* **198**, 82–87 (2000).
13. Zhou, S. *et al.* Fourier-based analysis of moiré fringe patterns of superposed gratings in alignment of nanolithography. *Opt. Express* **16**, 7869–7880 (2008).
14. Cowley, J. M. & Moodie, A. F. Fourier Images IV: the phase grating. *Proc. Phys. Soc. Lond.* **76**, 378–384 (1960).
15. Miao, H. *et al.* Enhancing tabletop X-ray phase contrast imaging with nano-fabrication. *Sci. Rep.* **5**, 13581 (2015).
16. Miao, H., Gomella, A. A., Chedid, N., Chen, L. & Wen, H. Fabrication of 200 nm period hard X-ray phase gratings. *Nano Lett.* **14**, 3453–3458 (2014).
17. Bruning, J. H. *et al.* Digital wavefront measuring interferometer for testing optical surfaces and lenses. *Appl. Opt.* **13**, 2693–2703 (1974).
18. Panna, A. *et al.* Performance of low-cost X-ray area detectors with consumer digital cameras. *J. Instrum.* **10**, T05005 (2015).
19. Yashiro, W. & Momose, A. Effects of unresolvable edges in grating-based X-ray differential phase imaging. *Opt. Express* **23**, 9233–9251 (2015).
20. Cowley, J. M. & Moodie, A. F. Fourier Images I: the point source. *Proc. Phys. Soc. Lond. B* **70**, 486–496 (1957).

## Acknowledgements

We are grateful to G. Melvin and D. Mazilu for mechanical design and machining, to M. Rivers, Department of Geophysical Sciences and Center for Advanced Radiation Sources, University of Chicago, for his help with the instrument control software. We thank R. Kasica and L. Yu of the Center for Nanoscale Science and Technology, National Institute of Standards and Technology, for their assistance with fabrication.

## Author contributions

H.M., A.P. and H.W. performed the experiments. H.M., L.C. and S.Z. performed fabrication. A.A.G., A.P., E.E.B., H.M. and H.W. built the systems. H.W. and H.M. performed the theoretical modelling and numerical calculations. H.W. and H.M. wrote the manuscript with input from all authors.

## Additional information

Supplementary information is available in the [online version of the paper](#). Reprints and permissions information is available online at [www.nature.com/reprints](http://www.nature.com/reprints). Correspondence and requests for materials should be addressed to H.M. or H.W.

## Competing financial interests

The authors declare no competing financial interests.

## Methods

**Theoretical modelling of the effect between two diffraction gratings.** The theory applies to the general case of a cone beam illuminating a pair of diffraction gratings of different periods with a possible spacing between them. The gratings can modulate the phase or amplitude (or both) of the beam. Two assumptions are made: the wavelength  $\lambda \ll$  grating periods; the gratings act as multiplicative transmission functions on the complex amplitude wavefront. The moiré effect is shown to be determined by auto-correlation functions of the grating transmission profiles.

Referring to the schematics of Fig. 1a, the scalar field at a point  $y$  on the image plane is given by the Fresnel–Kirchhoff diffraction integral<sup>20</sup>

$$V(y) \propto \iint \frac{1}{r_0 r_1 r_2} \exp[ik(r_0 + r_1 + r_2)] T_1(y_1) T_2(y_2) dy_1 dy_2 \quad (1)$$

where  $k$  is the wavenumber in vacuum,  $y_1$  and  $y_2$  are coordinates in the  $G_1$  and  $G_2$  planes;  $r_0$ ,  $r_1$  and  $r_2$  are the successive spacings between the source, the points  $y_1$ ,  $y_2$  and  $y$ , respectively;  $T_1$  and  $T_2$  are the complex grating transmission functions. They are further written in Fourier series as

$$T_1(y_1) = \sum A_m \exp(i2\pi m f_1 y_1) \quad (2)$$

and

$$T_2(y_2) = \sum B_n \exp(i2\pi n f_2 y_2) \quad (3)$$

where  $f_1$  and  $f_2$  are the spatial frequencies of the gratings. The vertical coordinate of the source is  $y_s$ . Substituting equations (2) and (3) into equation (1), expanding the phase factor of each  $A_m B_n$  term to the second order around its minimum point at  $\partial\phi/\partial y_i = 0$ , and carrying through the Fresnel integral leads to an explicit expression of the wave field

$$V(y) \propto \exp(ikL/\cos\theta) \sum_{m,n} A_m B_n \exp[i\Phi_0(m,n) + i\Phi_1(m,n)] \quad (4)$$

where  $\theta$  is the elevation angle of the line connecting the source to point  $y$  (Fig. 1a)

$$\begin{aligned} \Phi_0(m,n) = & 2\pi m f_1 \left( \frac{L_1}{L} y + \frac{D+L_2}{L} y_s \right) \\ & + 2\pi n f_2 \left( \frac{L_1+D}{L} y + \frac{L_2}{L} y_s \right) \end{aligned} \quad (5)$$

and

$$\begin{aligned} \Phi_1(m,n) = & -\frac{L}{2k\cos^3\theta} [(2\pi m f_1)^2 L_1/L \\ & + (2\pi n f_2)^2 L_2/L - (2\pi m f_1 L_1/L - 2\pi n f_2 L_2/L)^2] \end{aligned} \quad (6)$$

Considering the phase difference between the  $A_m B_n$  and the  $A_{m+1} B_{n-1}$  terms, which contains an achromatic part

$$\begin{aligned} \Phi_0(m,n) - \Phi_0(m+1,n-1) = & 2\pi \left( f_2 \frac{L_1+D}{L} - f_1 \frac{L_1}{L} \right) y \\ & + 2\pi \left( f_2 \frac{L_2}{L} - f_1 \frac{D+L_2}{L} \right) y_s \end{aligned} \quad (7)$$

and a wavelength-dependent part

$$\begin{aligned} \Phi_1(m,n) - \Phi_1(m+1,n-1) = & 2\pi \left( m + \frac{1}{2} \right) \delta_1(\lambda) \\ & - 2\pi \left( n - \frac{1}{2} \right) \delta_2(\lambda) \end{aligned} \quad (8)$$

where the increments are

$$\delta_1(\lambda) = \frac{\lambda}{L\cos^3\theta} f_1 L_1 [(f_1 - f_2)L_2 + f_1 D] \quad (9)$$

and

$$\delta_2(\lambda) = \frac{\lambda}{L\cos^3\theta} f_2 L_2 [(f_2 - f_1)L_1 + f_2 D] \quad (10)$$

The achromatic part (equation (7)) implies the potential for a moiré pattern at the image plane with a wavelength-independent period of

$$P_d = L/[(f_2 - f_1)L_1 + f_2 D] \quad (11)$$

The moiré fringes arise from the product of the  $A_m B_n$  and  $A_{m+1} B_{n-1}$  terms in the image intensity distribution of  $|V(y)|^2$ . Its complex amplitude according to equations (7) and (8) is

$$\begin{aligned} H_1(\lambda) \propto \exp \left[ i \left( \frac{2\pi y}{P_d} - \frac{2\pi y_s}{P_s} \right) \right] \sum_m A_m A_{m+1}^* e^{i2\pi(m+1/2)\delta_1} \\ \times \sum_n B_n B_{n-1}^* e^{-i2\pi(n-1/2)\delta_2} \end{aligned} \quad (12)$$

Noting that the phase of the pattern also depends cyclically on the source position with a period of

$$P_s = L/[(f_1 - f_2)L_2 + f_1 D] \quad (13)$$

this is called the source period. The summations in equation (12) are in fact Fourier coefficients of auto-correlation functions of the grating transmission profiles, known as the ambiguity function in waveform analysis:

$$\begin{aligned} \sum_m A_m A_{m+1}^* e^{i2\pi(m+1/2)\delta_1} &= \chi_1(\delta_1 P_1, f_1) \\ &= \frac{1}{P_1} \int_0^{P_1} T_1(\xi + \delta_1 P_1/2) T_1^*(\xi - \delta_1 P_1/2) \exp(i2\pi\xi f_1) d\xi \end{aligned} \quad (14)$$

and

$$\begin{aligned} \sum_n B_n B_{n-1}^* e^{-i2\pi(n-1/2)\delta_2} &= \chi_2^*(\delta_2 P_2, f_2) \\ &= \left[ \frac{1}{P_2} \int_0^{P_2} T_2(\xi + \delta_2 P_2/2) T_2^*(\xi - \delta_2 P_2/2) \exp(i2\pi\xi f_2) d\xi \right]^* \end{aligned} \quad (15)$$

Substituting equations (14) and (15) into equation (12) provides a closed-form expression of the moiré fringe contrast. The Fourier coefficient of the fringe amplitude normalized to the mean intensity is

$$\frac{H_1(\lambda)}{H_0} = \frac{\chi_1(\delta_1 P_1, f_1) \chi_2^*(\delta_2 P_2, f_2)}{\langle T_1 T_1^* \rangle \langle T_2 T_2^* \rangle} \quad (16)$$

where  $\langle T_j T_j^* \rangle$  denotes the average intensity transmission through a grating.

The fringe and source periods in equations (11) and (13) can be written in terms of the auto-correlation distances  $\delta_j(\lambda)$  as

$$P_d = \frac{1}{\delta_2(\lambda) \cos^3\theta} \frac{\lambda}{P_2} L_2 \quad (17)$$

and

$$P_s = \frac{1}{\delta_1(\lambda) \cos^3\theta} \frac{\lambda}{P_1} L_1 \quad (18)$$

Several physical facts of the universal moiré effect emerge from the formulae. For a polychromatic source, the fringe contrast is a weighted average of equation (16) over the light spectrum. The key determinant of the moiré effect is the auto-correlation distances  $\delta_j(\lambda)$ . The equations indicate a trend of decreasing fringe contrast with increasing spectral spread of  $\delta_j(\lambda)$  when the spacing  $D$  is enlarged. This is seen in the data in Fig. 2b. Owing to the cyclic dependence of the ambiguity functions on the auto-correlation distances, the fringe contrast oscillates with the spacing  $D$ , as seen in Fig. 2b. Because the auto-correlation distances depend on both the grating period differential  $f_1 - f_2$  and their spacing, there are a continuous range of conditions for significant moiré effects. In the example of Fig. 2, a small gap between two gratings of the same period produces the effect. Alternatively, if two gratings are overlaid with no spacing, a proper difference in periods also maximizes the moiré fringes. The fringe period scales linearly with the  $G_2$ -to-image distance and inversely with the grating period. An extreme case is when  $G_2$  is an amplitude grating which produces a moiré pattern at  $\delta_2 = 0$ . It describes the classic moiré effect appearing immediately behind  $G_2$ . With a finite-sized source, the fringe amplitude is the integral of equation (12) over the source distribution. For a significant moiré effect the source size  $S$  should be less than half the source period  $P_s$ . Equivalently, the lateral coherence of the source at the first grating,  $\lambda L_1/S$ , should be greater than  $2\delta_1 P_1$ . The extreme is when  $G_1$  is an amplitude grating, which produces a moiré effect at  $\delta_1 = 0$ . In this case there is no limit on the source size because  $G_1$  filters the source into a set of line sources.

**Modelling of the three-grating system.** Here the first two gratings are widely separated (Fig. 3a). Previous equations for the two-grating system describe the wavefront before the third grating. Consider the phase difference between the  $A_m B_1$  and  $A_{m+1} B_{-1}$  terms of the wave amplitude (equations (4)–(6)). It is independent of

wavelength and invariant with the diffraction order  $m$  at a specific 'echo' plane at a distance  $L_2$  downstream from the  $G_2$  grating, where

$$L_2 = D_1[f_1/(2f_2 - f_1)] \quad (19)$$

At the echo plane the wave amplitude contains the sum of pairs as

$$V_E(y) \propto \exp(ikL \cos^3 \theta) \times \sum_m e^{i[\phi_0(m,1) + \phi_1(m,1)]} [A_m B_1 + A_{m+1} B_{-1} e^{i2\pi(f_1 - 2f_2)y}] \quad (20)$$

Each pair represents an achromatic interference pattern superimposed onto a spherical wave, or a Fourier image<sup>20</sup> from  $G_1$ . For a polychromatic source the pairs are mutually incoherent owing to the strong wavelength dependence of  $\phi_1(m,1)$  (equation (6)). When a third grating  $G_3$  is placed on or near the echo plane, and its frequency  $f_3$  is near  $2f_2 - f_1$ , each Fourier image forms a moiré pattern with  $G_3$  at the image plane further downstream. The incoherent sum of these moiré patterns is the overall moiré pattern. Referring to Fig. 3a for geometric parameters, the normalized moiré fringe amplitude is given by

$$\frac{H_1(\lambda)}{H_0} = \frac{\chi_1(\delta_1 P_1, f_1)}{\langle T_1 T_1^* \rangle} B_1 B_{-1}^* \frac{\chi_3(\delta_3 P_3, f_3)}{\langle T_3 T_3^* \rangle} \quad (21)$$

where the fractional auto-correlation distances are

$$\delta_1(\lambda) = \lambda \frac{f_1 L_1}{L \cos^3 \theta} [(f_1 - f_2)(L - L_1) + (f_3 - f_2)L_3 - f_2(D_3 - D_1)] \quad (22)$$

and

$$\delta_3(\lambda) = \lambda \frac{f_3 L_3}{L \cos^3 \theta} [(f_3 - f_2)(L - L_3) + (f_1 - f_2)L_1 - f_2(D_1 - D_3)] \quad (23)$$

Similar to the two-grating case, the moiré fringe period and the source period are both independent of wavelength:

$$P_d = L / [(f_3 - f_2)(L - L_3) + (f_1 - f_2)L_1 - f_2(D_1 - D_3)] \quad (24)$$

and

$$P_s = L / [(f_1 - f_2)(L - L_1) + (f_3 - f_2)L_3 - f_2(D_3 - D_1)] \quad (25)$$

The physical effects described by these results are similar to the two-grating case. With a polychromatic source the moiré effect is maximized for a specific set of auto-correlation distances  $\delta_i(\lambda)$ , which can be adjusted by the position of the third grating  $G_3$ , as seen in Fig. 4b; tilting the  $G_1$  and  $G_3$  gratings out of plane alters their transmission profiles, which changes the moiré fringe amplitude in a predictable way, as shown in Fig. 4c,d; the moiré fringe period scales linearly with the  $G_3$ -to-image distance and inversely with the grating periods; the extreme case of significant moiré fringes at  $\delta_3 = 0$  when  $G_3$  is an amplitude grating describes the classic moiré effect which appears immediately behind  $G_3$ ; the source size should be less than half the source period  $P_s$ , or equivalently the lateral coherence of the source at the first grating,  $\lambda L_1/S$ , should be greater than  $2\delta_1 P_1$ ; the extreme case of a moiré pattern at  $\delta_1 = 0$  when  $G_1$  is an amplitude grating describes the source being filtered by  $G_1$  into a set of line sources.